Nanoscale

PAPER

View Article Online
View Journal | View Issue

Cite this: *Nanoscale*, 2019, **11**, 18874

Plasmonic hot electron transfer in anisotropic Pt–Au nanodisks boosts electrochemical reactions in the visible-NIR region†

Guanying Chen,[a] Mingjuan Sun,[b] Juan Li,[a] Mingshan Zhu,*[b] Zaizhu Lou*[a] and Baojun Li[a]

Anisotropic plasmonic metals have attracted significant attention in enhancing the catalytic performance of catalysts due to their broad light-harnessing capabilities and active hot electrons; however, limited investigations have been dedicated towards improving their electrochemical reaction performance in the visible and near infrared (NIR) regions. Herein, anisotropic Pt-edged Au nanodisks (NDs) were synthesized by controlling the preferential loading of Pt and used as catalysts for plasmon-enhanced electrochemical methanol oxidation reactions (MORs) under visible-NIR light irradiation by, and the light-enhanced electric current over the Pt-edged Au NDs was found to be 3-fold higher than that under dark conditions. Wavelength-dependent electric current over the Pt-edged Au NDs for the MOR in the visible-NIR light region demonstrates that the light-induced enhancement of the electric current is due to surface plasmon resonance (SPR) of the Au NDs. Furthermore, plasmonic hot electron transfer was studied by the single-particle photoluminescence images and spectra of Au NDs and Pt–Au NDs, and the dipole surface plasmon resonance (DSPR) mode was proved to be the main channel for hot electron transfer. During the electrochemical reaction under visible-NIR light irradiation, a plasmonic hot electron is transferred to the electrode, and a "hot hole" is left on the surface, boosting the MOR.

Received 26th July 2019,
Accepted 23rd September 2019

DOI: 10.1039/c9nr06372b

rsc.li/nanoscale

1. Introduction

Surface plasmon resonance (SPR) having strong interactions with visible-near-infrared (NIR) light has been utilized in various fields including cancer therapy,[1,2] optical detection,[3,4] chemical analysis[5,6] and Raman signal enhancement.[7,8] The SPR of noble metal nanoparticles (NPs) is sensitive to their compositions, surrounding environment and, especially, their shapes.[9–11] Thus, many structures (nanospheres, nanorods, nanowires, *etc.*) of Au NPs with strong SPR have been synthesized for applications. Among these, two-dimensional (2D) nanostructures (nanoprisms and nanodisks) with large surface polarization as anisotropic structures have multipolar resonance modes and tunable plasmonic bands in the visible and NIR regions.[12] SPR-induced hot electron transfer has been studied in plasmonic metal/semiconductor heterostructures.[13,14] Anisotropic Pt–Au nanostructures of nanoprisms were synthesized as plasmonic photocatalysts for water splitting; moreover, fast hot electron transfer between Pt and Au was demonstrated by single-particle photoluminescence (PL) microscopy, boosting hydrogen generation under light irradiation.[15,16] With dipole and multipolar resonance modes, Au triangular nanoprisms provide multi-channels for hot electron transfer in Pt-nanoframe/reduced graphene/Au-nanoprism and Ag_2S-edged Au nanoprism heterostructures, resulting in higher photocatalytic performance than those of Au nanospheres and nanorods.[17] The sharp corners of Au triangular nanoprisms have large curvatures and have been demonstrated to have a strong interaction with incident light to generate hot electrons for transfer. However, the small areas of the sharp corners in triangular nanoprisms limit efficient hot electron generation. Contrary to triangular particles, Au nanodisks have large edge areas and strong plasmonic electrical fields to generate hot electrons, which enable the construction of more anisotropic structures for catalysis by promoting the plasmonic hot electron transfer.

Noble metal NPs (PtNPs, PdNPs, *etc.*) are well-known catalysts for chemical reactions, especially Pt, which is an excellent co-catalyst for photocatalytic hydrogen evolution.[18–20] Pd also exhibits high activity in organic synthesis.[21,22] However, most active metal (Pt and Pd) NPs have weak SPR effects, whereas

[a]*Institute of Nanophotonics, Jinan University, Xingye Avenue East 855, Guangzhou 511443, China. E-mail: zzlou@jnu.edu.cn*
[b]*School of Environment, Jinan University, Xingye Avenue East 855, Guangzhou 511443, China. E-mail: mingshanzhu@yahoo.com*

†Electronic supplementary information (ESI) available. See DOI: 10.1039/c9nr06372b

strong SPR metal (Au and Ag) NPs show low activity in catalysis.[23] Thus, one strategy to obtain both high catalytic activity and strong SPR is constructing bimetallic or multimetallic structures. For example, Au–Pd bimetallic superstructures with strong plasmonic effects and high catalytic activity were synthesized by Tang's group; they exhibited 201% SPR-enhancement in light-driven catalysis.[24] Pt-tipped Au nanorods were demonstrated to show efficient charge separation and plasmonic hot electron transfer, enhancing photocatalytic hydrogen generation.[25] The above investigations reveal that optical excitation by plasmonic NPs can convert photonic energy to plasmonic energy, resulting in activated and accelerated photocatalysis. To date, a growing number of examples have focused on plasmon-enhanced photocatalysis; meanwhile, few reports have been published on SPR-enhanced electrochemical reactions with broad light harvesting, especially in the NIR region, and the detailed mechanism is still unclear.

In this work, anisotropic Pt-edged Au nanodisks were synthesized by controlling the overgrowth of Pt on the edges of Au nanodisks as a catalyst for the plasmon-enhanced electrochemical methanol oxidation reaction (MOR) under visible-NIR light illumination; they exhibited greatly SPR-enhanced electrochemical activity. To the best of our knowledge, this study presents the first investigation of a plasmon-enhanced electrochemical reaction in the visible-NIR region. The influence of the size of the Au NDs on MOR was investigated; it was demonstrated that the optimal size of 66 nm exhibited strong SPR and a greater active area for reaction. The wavelength-dependent electric current for MOR verified that the enhanced electrochemical catalysis is due to the SPR of the Au NDs. Single-particle studies of the PL spectra and images of an individual Au ND and Pt-edged Au ND demonstrated that dipole surface plasmon resonance (DSPR) is the main channel for the plasmonic hot electron transfer. Plasmonic hot electron on Pt joins the external circuit driven by the positive potential, while the "hot hole" is left on the surface to play the dominant role in MOR.

2. Experimental

Materials

Hexadecyltrimethylammonium bromide (CTAB, ≥97%, Aladdin), hexadecyltrimethylammonium chloride (CTAC, ≥97%, Aladdin), sodium borohydride ($NaBH_4$, ≥98%, Aladdin), $HAuCl_4{\cdot}H_2O$ (≥99.995%, Sigma-Aldrich), silver nitrate (≥99.9%, Alfa Aesar), ascorbic acid (≥99%, Aladdin), KI (≥99.99%, Aladdin), and $H_2PtCl_6{\cdot}nH_2O$ (≥99.9%, Sigma-Aldrich) were used. Ultrapure water at room temperature was used in the experiments.

Synthesis of Au NDs

Firstly, Au TNPs were synthesized with uniform dispersions as a precursor by the seed-growth chemical method, as reported in previous work.[15] In a typical procedure, the precipitate was separated from 10 mL Au TNPs CTAC (20 mM) solution by centrifugation at 6000 rpm for 20 min and was then dispersed in 10 mL 20 mM CTAB solution. A total of 1 mL etching solution was prepared with 10 μL $HAuCl_4$ (50 mM) and 0.5 mL CTAB (0.1 M). 10 μL KI (10 mM) and 0.3 mL etching solution were mixed with Au TNPs solution and left for one hour. After that, the solution was centrifuged at 7000 rpm for 20 min. After the supernatant solution was removed, the precipitate was dispersed in 10 mL 20 mM CTAB solution. The pure Au NDs were obtained. Different sizes of Au NDs were obtained by adding various amounts of etching solution.

Synthesis of Pt-edged Au NDs

Typically, 100 μL KI (10 mM), 30 μL NaOH (0.1 M), 20 μL $AgNO_3$ (20 mM), and 0.2 mL ascorbic acid (0.1 M) were added to 10 mL Au NDs solution. The mixed solution was maintained at 70 °C for one hour in a water bath. Then, 15 μL H_2PtCl_6 (10 mM) was added, and the solution was maintained at 70 °C for two hours. Finally, Pt was edged on the NDs.

FDTD simulations

The calculation simulations of Au NDs, Pt-edged Au NDs, and Pt NFs were carried out using finite-difference-time-domain (FDTD) studies. A software package with the FDTD solution (Lumerical Solution, Inc.) was used for the simulations. The optical constant of the gold circular nanodisk was bulk gold as measured by Johnson and Christy. The override mesh cell was set to $1 \times 1 \times 1$ nm^3. The diameter and thickness of the Au ND were set to 75 and 6 nm, respectively. The orientation of incident light polarization was set in the horizontal direction.[12] For the model of the Pt-edged Au ND, a ring with a diameter of 7 nm was located at the edge of the ND, and the thickness was the same as that of the Au ND. For the model of the NF, the parameters were the same as for the Pt-edged Au ND. The models were simulated in aqueous solutions with a refractive index of 1.33.

Photoelectrochemical methanol oxidation reaction

The photoelectrocatalytic reaction was studied using an electrochemical workstation (CHI 760E) in a standard three-electrode system. A platinum wire, saturated calomel electrode (SCE) and the as-prepared modified electrode were used as the counter, reference and working electrodes, respectively. The photoelectrocatalytic activity of methanol was measured by cyclic voltammetry measurements at a scan rate of 50 mV s^{-1}. The chronopotentiometry curves of the Pt-edged Au NDs electrode were measured at a current density of 1 μA under visible-NIR light illumination and in dark conditions. The working electrode was irradiated for the photo-electrochemical measurements. Visible-NIR light was supplied by a xenon lamp (300 W) equipped with a UV cut–off filter (>420 nm).

Single-particle PL measurements

Au NDs (66 nm) and Pt-edged NDs were separated by centrifugation at 6000 rpm from solution and then were washed with ultrapure water three times and redispersed in ultrapure water. Au NDs aqueous suspensions were loaded on a cover glass using spin-coating; then, the cover glass was transferred into

an oven at 80 °C for 30 min. PL spectra and images of the samples at the single-particle level were measured using an Olympus IX71 inverted fluorescence microscope coupled with an objective scanning confocal microscope system (PicoQuant, MicroTime 200). A circular-polarized 405 nm continuous-wave laser controlled by a PDL-800B driver (PicoQuant) was used to excite the samples through an oil-immersion objective lens (Olympus, UplanSApochromat, 100×, 1.4NA), and the excitation power was controlled to be 200 μW for the PL measurements. The emissions of the samples were collected by the same objective and the images were detected by a single photon avalanche photodiode (PDM 50CT) through a dichroic beam splitter (Chroma, 405rdc) and long pass filter (Chroma, HQ430CP). An imaging spectrograph (Acton Research, SP-2356) equipped with an electron-multiplying charge-coupled device (EMCCD) camera (ProEM) was used to collect the PL spectra with typical integration for 10 s. The experimental data were obtained at room temperature and analysed using a personal computer.

Characterization

The morphologies of the samples were measured using a transmission electron microscope (TEM, JEOL, 2100, operated at 100 kV). Optical extinction spectra were recorded by a Cary Series UV-Vis-NIR spectrophotometer. The mass concentrations of gold and platinum were measured by an ICP-AES device (iCAP6500Duo, ThermoFisher).

3. Results and discussion

Gold triangular nanoprisms (TEM image in Fig. S1†) with lengths and thicknesses of 140 and 7 nm, respectively, were synthesized firstly as a precursor according to our previous work;[26] then, a wet chemical etching method was used to control the preferential etching on the three corners. More details are shown in the Experimental section. Finally, uniform nanodisks (NDs, size of 75 nm) were obtained, as shown in the TEM images in Fig. 1a and b. The size distribution was calculated as shown in Fig. S2a.† Then, the preferential overgrowth of Pt on the Au NDs was controlled using KI reagent to limit the growth of Pt on their (111) surfaces; Pt-edged Au NDs with anisotropic structures were obtained, as shown in the TEM images (Fig. 1c and d). The growth of Pt was located on the edges of the Au NDs, and the high resolution TEM (HRTEM) images further verified their anisotropic structures (Fig. 1e). The lattice spacing of 0.138 nm is located on the edge corresponding to the (220) plane of Pt; meanwhile, the lattice spacing of 0.144 nm is located on the surface corresponding to the (220) plane of Au, demonstrating the location of Pt on the edges.[27] For reference, the Pt-edged Au NDs were etched with $HAuCl_4$ in solution to remove Au, and Pt nanoframes (NFs) were obtained, as shown in the TEM image in Fig. 1f.

In the visible-NIR extinction spectrum of the Au NDs (Fig. 2a), only one SPR band around 835 nm is observed,

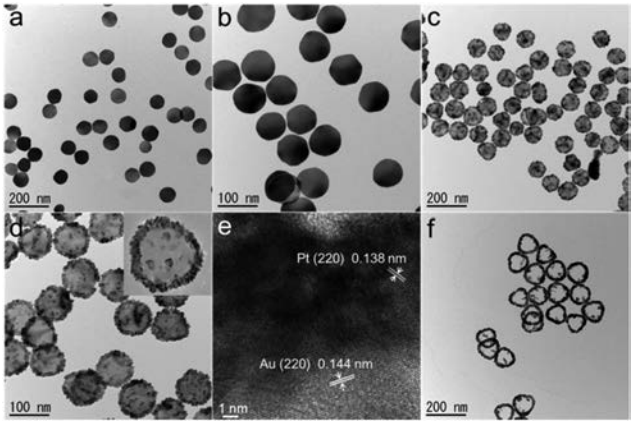

Fig. 1 TEM and HRTEM images of Au NDs (a and b), Pt-edged Au NDs (c, d, and e) and Pt NFs (f).

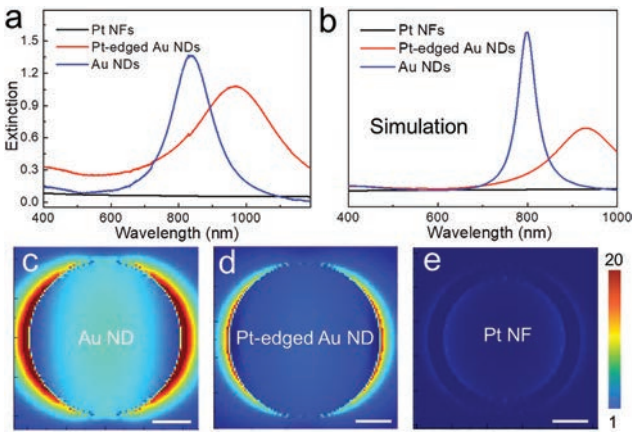

Fig. 2 Experimental (a) and FDTD-simulated (b) extinction spectra of the Au NDs, Pt-edged Au NDs and Pt NFs. FDTD-simulated plasmon-induced electrical field distributions on an Au ND (c), Pt-edged Au ND (d) and Pt NF.

corresponding to in-plane dipole surface plasmon resonance (DSPR).[28] The mutlipolar plasmon resonance (MSPR) band of the Au triangular nanoprisms (Fig. S3†) disappeared, suggesting the formation of ND structures. When Pt was loaded on the edges of the Au NDs, the DSPR band showed a red shift to 970 nm. Meanwhile, the SPR band intensity decreased due to the strong ohmic loss of Pt loaded on the edges of the Au NDs. The broader SPR band is due to the loading of Pt on the Au NDs.[29] When Au was completely removed from the Pt-edged Au NDs, no SPR band was observed for the Pt-NFs. The calculated extinction spectra of the Au NDs, Pt-edged Au NDs and Pt NFs were simulated using the Finite-Difference Time-Domain (FDTD) method, as shown in Fig. 2b. Au ND, Pt-edged Au ND and Pt NF modes were constructed, as shown in Fig. S4.† Their calculated spectra are consistent with the experimental spectra. The distributions of the plasmon-induced electrical field on the different structures were also simulated by FDTD, as shown in Fig. 2c–e. For the

pure Au NDs, the strongest electrical field is distributed on the edges of the NDs, where high curvature and surface polarization are present (Fig. 2c). When Pt was selectively loaded on the edges of the Au NDs, the SPR band intensity of the Au NDs decreased (Fig. 2a and b); however, the plasmon-induced electrical field on the Pt-edged Au NDs remained strong (Fig. 2d). Without SPR, no plasmon-induced electrical field was observed on the Pt NFs (Fig. 2e). Consequently, the anisotropic Pt-edged Au NDs have both the SPR of Au and the catalytic activity of Pt.

To investigate the plasmon-enhanced electrocatalytic activity over the Pt-edged Au NDs, Pt NFs and Au NDs, the photoelectrochemical oxidation of methanol under alkaline conditions was measured. Fig. 3a shows the cyclic voltammetry (CV) curves of the Pt NFs and Pt-edged Au NDs-modified electrodes for the electrochemical oxidation of methanol under visible-NIR light illumination and in dark conditions. Firstly, in dark conditions, the two characteristic oxidation peaks, *viz*. the forward curve and the backward curve, were observed at *ca.* −0.3 V and *ca.* −0.5 V, respectively. The forward peak current density of the Pt-edged Au NDs-modified electrode is 0.79 mA cm^{-2}. When the electrode was subjected to visible-NIR light illumination, the forward peak current density highly improved by 3.3 times, suggesting that the photo-assisted process is beneficial for electrocatalytic methanol oxidation. The CV curves (Fig. S5†) of the Au NDs-modified electrodes for the electrochemical oxidation of methanol under visible light illumination and dark conditions show their low activity in methanol oxidation. Fig. 3b shows a summary of the forward peak current densities of the Pt NFs, Pt-edged Au NDs and Au NDs-modified electrodes under visible-NIR light illumination and in dark conditions. It can be clearly seen that the pure Pt NFs and Au NDs have very low performance in electrocatalytic methanol oxidation in both light irradiation and dark conditions. However, the photoelectrocatalytic activity of the Pt-edged Au NDs is distinctly improved; this can be attributed to the greater number of plasmonic "hot holes" existing on the surface, which enhanced the electrochemical reaction.[30,31]

The SPR of the Au NDs is sensitive to their sizes because of surface polarization, resulting in a tunable SPR band in the visible-NIR region. Au NDs with different sizes were synthesized by controlling the etching reagent ($HAuCl_4$ solution) volume, and TEM images of the obtained NDs structures are shown in Fig. S5.† The average sizes of the Au NDs (see the size distribution diagram in Fig. S2†) were calculated to be 54, 57, 66, and 70 nm, respectively. From their extinction spectra (Fig. S6e†), as the size decreases, the SPR band undergoes a blue shift with decreased intensity, which can be attributed to the decreased ratio of length/thickness. After Pt was loaded, TEM images of the Pt-edged Au NDs with different sizes are shown in Fig. S7a–d,† and it can be observed clearly that Pt is loaded on the edges of the Au NDs. In contrast to the Au NDs, the extinction spectra (Fig. S7e†) of the Pt-edged NDs all show red shifts and decreased intensities, demonstrating the edge-loading of Pt. SPR-induced electrical field distributions on different Au NDs and Pt-edged NDs were simulated, as shown in Fig. S8 and S9.† The great differences in the SPR spectra of the Pt-edged Au NDs have influences on the photo-enhanced electrochemical methanol oxidization.

The electrochemical oxidation of methanol over the different Pt-edged Au NDs was measured, and the CVs are shown in Fig. S10.† For comparison, the CV oxidation peak current densities over the different samples are summarized in Fig. S11a.† In the dark, the current decreased with decreasing size of the Au NDs. Upon visible-NIR light irradiation, the CV oxidation peak current densities greatly increased compared to those in the dark. As the size decreases, the light-induced enhancement of the CV oxidation peak current weakens, which demonstrates the SPR-induced promotion of methanol oxidation. Fig. S11a† shows the obtained results with the same particle numbers in the samples. The actual Au amounts were measured by ICP to be 0.0395, 0.0242, 0.0151, 0.0119 and 0.0058 mg for the samples with sizes of 75, 70, 66, 57 and 54 nm, respectively. Fig. S11b† shows the CV oxidation peak current densities over different samples whose actual Au amounts were normalized to 0.0395 mg. The enhanced CV oxidation peak current densities were calculated to be 1.821, 1.787, 2.075, 1.328 and 1.652 mA cm^{-2} for the samples with sizes of 75, 70, 66, 57 and 54 nm, respectively. The CV oxidation peak current densities over the different samples were normalized by the actual Pt amount, as shown in Fig. S12;† the results indicated that their peak current densities are consistent with the intensities of their SPR bands. Consequently, the Pt-edged Au NDs with sizes of 66 nm are the proper structure to obtain optimal SPR-enhancement of methanol oxidation. It is known that SPR has two effects: electron–hole generation and photothermal effects.[32] Plasmonic electron–hole generation is considered to play the dominant role in enhancing methanol oxidation. The Au NDs with large sizes have a SPR band red shift to the NIR, resulting in strong photothermal effects, while the NDs with small sizes have a SPR blue shift, resulting in weak SPR bands. Considering these two points, the Au NDs with a size of 66 nm are the optimal structures with strong SPR to enhance plasmonic electron–hole generation for methanol oxidation.

To further demonstrate the SPR-induced enhancement of methanol oxidation, wavelength-dependent methanol oxidation over Pt-edged Au NDs (66 nm) was investigated, as shown in Fig. 4a and b. Under 850 nm light irradiation around the SPR band center, CV of the samples shows the highest

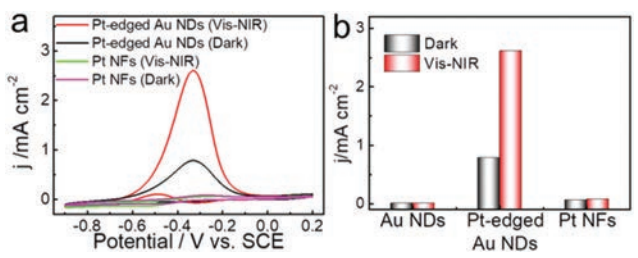

Fig. 3 Methanol electrocatalytic oxidization CVs (a) and oxidation peak intensities (b) over different catalysts of Pt NFs, Pt-edged Au NDs and Au NDs under visible-NIR light illumination and in the dark.

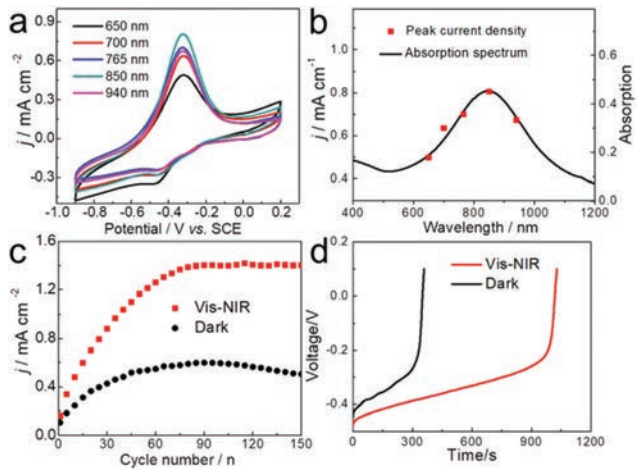

Fig. 4 CV (a) of the Pt-edged Au NDs under different wavelengths of light illumination using band pass filters. The wavelength-dependent mass activities of MOR and the optical absorption of the Pt-edged Au NDs (b). The peak current in the forward scan *vs.* the CV cycle number (c) and the chronopotentiometry curves at 1 μA (d) of the Pt-edged Au NDs in 1.0 M CH_3OH + 1.0 M KOH solution under visible-NIR light illumination and in dark conditions.

current density on the methanol oxidation peak. Different wavelengths of light irradiation were applied, and the wavelength-dependent oxidation peak currents are summarized in Fig. 4b. It is clear that the changes in the wavelength-dependent current show the same trend as the SPR band of the Pt-edged Au NDs, strongly verifying that the methanol oxidation CV current enhancement results from SPR of the Au NDs.

The long-term stability of a catalyst is crucial to evaluate its potential as an electrocatalyst in practical applications. To investigate the stability of the Pt-edged Au NDs, scan cycling experiments together with chronopotentiometry curves were measured in CH_3OH (0.1 M) + KOH (1.0 M) solution under visible-NIR light illumination and in dark conditions, and the results are shown in Fig. 4c. The oxidation peak current densities of the Pt-edged Au NDs increased gradually with increasing cycle number at first, and the highest current was reached at the 90^{th} cycle. Then, the oxidation peak current density decreased by 15.7% after 150 cycles compared with the maximum current (0.599 mA cm^{-2}). However, for the Pt-edged Au NDs-modified electrode under visible-NIR light conditions, the oxidation peak current density was much higher and more steady; the highest oxidation peak current density was 1.4 mA cm^{-2} at the 90^{th} cycle, and after that its catalytic performance remained steady. This result suggests that the photoelectrocatalytic activity and stability of the Pt-edged Au NDs were highly enhanced with the assistance of visible-NIR light illumination.

To further confirm that photo-irradiation is beneficial for the durability of the Pt-edged Au NDs, the chronopotentiometry curves were studied at a current density of 1 μA under visible-NIR light irradiation and in dark conditions (Fig. 4d). Usually, the potential gradually increases with polarization time in the chronopotentiometry curves. When the voltage increases rapidly, it indicates that the catalyst has begun to be poisoned; therefore, a longer polarization time constant indicates that the catalyst has better poisoning tolerance. As shown in Fig. 4d, the Pt-edged Au NDs remained stable for 1029 s under visible-NIR light illumination, which is almost 2.86 times longer than the same electrode under dark conditions (360 s). These results indicate that the Pt-edged Au NDs-modified electrode has better poisoning resistance ability under visible-NIR light irradiation, which contributes to higher catalytic performance.

To demonstrate the hot electron generation, transfer and recombination on the Au NDs and Pt-edged Au NDs, an advanced confocal microscopy system was used for single-particle PL studies of individual samples. Au NDs (66 nm) were coated on a cover glass in a single-particle dispersion, and a 405 nm laser was used as an excitation source. A single-particle PL image of individual Au NDs is shown in Fig. 5a, and each brightness point corresponds to one Au ND particle. Single-particle PL spectra (Fig. 5b) corresponding to the numbered points in Fig. 5a show that one strong PL band around 750 nm is observed for eight Au ND particles, and the band arises from emission from SPR-induced carrier recombination on the DSPR band. The slight differences in the PL band positions are due to the different sizes of the particles. Because the PL measurements were carried out in air, the PL band positions have blue shifts compared to the SPR spectra (835 nm) of Au NDs in solution. When Pt is loaded, the brightness of a single-particle PL image (Fig. 5c) becomes dark, which indicates that PL quenching has occurred. The detailed PL quenching process was studied by the single-particle PL spectra in Fig. 5d. The DSPR PL intensity shows a great decrease, and a weak band was observed around 550 nm corresponding to

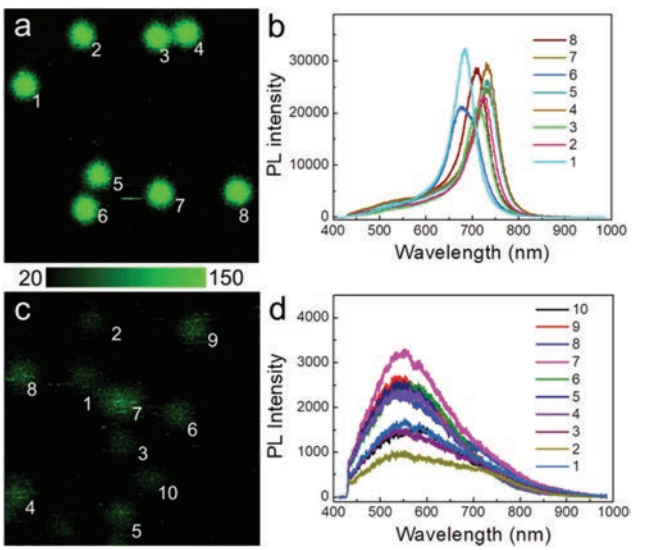

Fig. 5 Single-particle PL image (a) and spectra (b) of Au NDs. Single-particle PL image (c) and spectra (d) of Pt-edged Au NDs. Excitation: 200 μW 405 nm laser.

DSPR out-of-plane (DSPR-O), which was also observed in the PL spectra of the Au NDs (Fig. S13†) The quenching efficiencies of DSPR and DSPR-O PL were calculated to be 96.3% and 9.6%, respectively. Therefore, DSPR is the main channel for PL quenching, demonstrating that SPR-induced hot electrons transfer from Au to Pt in the anisotropic Pt-edged Au NDs.

The mechanisms of SPR-induced hot electron generation, transfer and recombination in the Au NDs are described in Scheme 1. Under 405 nm laser excitation, the electron in the ground state of Au is excited to undergo an interband transition (blue line) at a high energy level; then, the excited hole–electron pairs undergo energy transfer to the DSPR-O band and emit one photon in the short (bright green line, 550 nm) wavelength region, and weak DSPR-O leads to weak DSPR-O PL bands. Meanwhile, DSPR is the strong SPR mode that acts as the dominant energy transfer channel for radiative decay, resulting in strong DSPR emission (bright red line) in the long wavelength (750 nm) region.[33] After Pt is loaded, the occurrence of PL quenching demonstrates that the hot electron transfers from Au to Pt for charge separation, and a "hot hole" is left on Au.[34,35] Under visible-NIR light irradiation, excitations of the interband transition, DSPR-O and DSPR can all generate hot electrons, which undergo energy transfer to collect on the DSPR and transfer to Pt for charge separation; this restricts the radiative decay of hole–electron pairs on the DSPR. The reaction mechanism of photoelectrochemcial methanol oxidation is described in Scheme 1 (below). SPR induces hot electrons and "hot holes" on the Au NDs. After charge separation, the hot electrons on Pt have two possible transfer channels: (1) recombining with holes to undergo non-radiative decay and (2) entering the external circuit, driven by the positive potential.[32,36] After the hot electron is removed, the "hot hole" is left on the surface of the Au ND for methanol oxidation, leading to enhanced oxidation current for methanol oxidation. Furthermore, compared to the potential-driven oxidation in the dark, the plasmon-induced "hot hole" is highly active for methanol oxidation by decreasing the reaction energy barriers.[37,38] For Au NDs, the lifetime of plasmon-induced hole–electron pairs is too short to enable charge separation and a few "hot holes" can be left on the surface for methanol oxidation, resulting in low activity in the photoelectrochemical reaction.

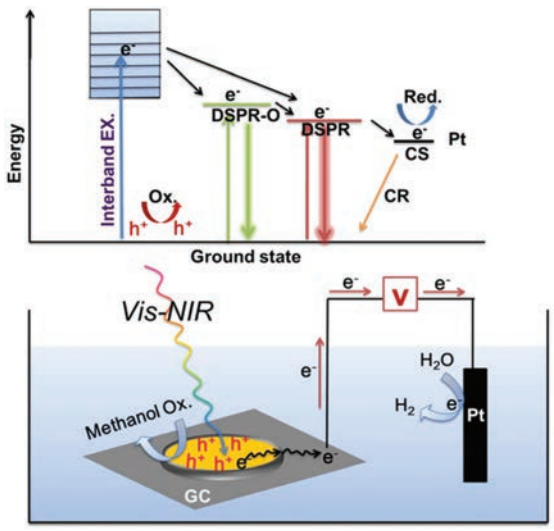

Scheme 1 Schematic of the radiative decay of SPR excitation (above) and reaction mechanism of photoelectrochemical methanol oxidation over the Pt-edged Au NDs (below). CS: charge separation, CR: charge recombination.

4. Conclusions

In summary, anisotropic Pt-edged Au NDs were synthesized by the preferential overgrowth of Pt on Au NDs and were used as catalysts for plasmon-enhanced electrochemical reactions. Under visible-NIR light illumination, the electric current over the Pt-edged Au NDs during methanol oxidation was greatly enhanced by three-fold. Pt-edged Au NDs with sizes of 66 nm were found to exhibit optimal enhancement of the SPR-induced activity. The wavelength-dependent electric currents of methanol oxidation showed a similar trend to that of SPR absorption, verifying that the light-induced enhancement of electric current is due to the SPR of the Au NDs. Single-particle PL spectra and image studies of the Au NDs and Pt-edged Au NDs demonstrate that DSPR is the main channel for PL quenching and that plasmonic hot electrons can transfer from Au to Pt for charge separation. Compared to the Au NDs, the Pt-edged Au NDs have efficient charge separation, leaving more active hot holes on the surface for methanol oxidation and resulting in greatly enhanced electric current. This work demonstrates that the bimetallic structure can promote plasmon-induced hot hole–electron separation to enhance photoelectrocatalytic reactions under visible-NIR irradiation.

Conflicts of interest

There are no conflicts to declare.

Acknowledgements

This work was supported by the National Natural Science Foundation of China (No. 21703083, 51872125 and 11804120), the Guangdong Natural Science Funds for Distinguished Young Scholar (2018B030306004), the Natural Science Foundation of Guangdong Province (2017A030310463) and the Project supported by GDUPS (2018).

Notes and references

1 Y. Chang, Y. Cheng, Y. Feng, H. Jian, L. Wang, X. Ma, X. Li and H. Zhang, *Nano Lett.*, 2018, **18**, 886–897.

2 X. Ding, C. H. Liow, M. Zhang, R. Huang, C. Li, H. Shen, M. Liu, Y. Zou, N. Gao, Z. Zhang, Y. Li, Q. Wang, S. Li and J. Jiang, *J. Am. Chem. Soc.*, 2014, **136**, 15684–15693.
3 K. Sadani, P. Nag and S. Mukherji, *Biosens. Bioelectron.*, 2019, **134**, 90–96.
4 Z. Ni, L. Ma, S. Du, Y. Xu, M. Yuan, H. Fang, Z. Wang, M. Xu, D. Li, J. Yang, W. Hu, X. Pi and D. Yang, *ACS Nano*, 2017, **11**, 9854–9862.
5 X. Ma, Y. Lin, L. Guo, B. Qiu, G. Chen, H. Yang and Z. Lin, *Biosens. Bioelectron.*, 2017, **87**, 122–128.
6 H. Aldewachi, T. Chalati, M. N. Woodroofe, N. Bricklebank, B. Sharrack and P. Gardiner, *Nanoscale*, 2018, **10**, 18–33.
7 Z. Huang, G. Meng, X. Hu, Q. Pan, D. Huo, H. Zhou, Y. Ke and N. Wu, *Nano Res.*, 2019, **12**, 449–455.
8 Y. H. Lee, C. K. Lee, B. Tan, J. M. R. Tan, I. Y. Phang and X. Y. Ling, *Nanoscale*, 2013, **5**, 6404–6412.
9 R. Shi, Y. Cao, Y. Bao, Y. Zhao, G. I. N. Waterhouse, Z. Fang, L. Wu, C. Tung, Y. Yin and T. Zhang, *Adv. Mater.*, 2017, **29**, 1700803.
10 H. Jang, S. Ham, J. A. I. Acapulco, J. Y. Song, S. Hong, K. L. Shuford and S. Park, *J. Am. Chem. Soc.*, 2014, **136**, 17674–17680.
11 S. Hong, K. L. Shuford and S. Park, *Chem. Mater.*, 2011, **23**, 2011–2013.
12 Z. Lou, S. Kim, P. Zhang, X. Shi, M. Fujitsuka and T. Majima, *ACS Nano*, 2017, **10**, 968–974.
13 K. Wu, J. Chen, J. R. McBride and T. Lian, *Science*, 2015, **349**, 632–635.
14 J. Zhou, J. Zhang, H. Yang, Z. Wang, J. Shi, W. Zhou, N. Jiang, G. Xian, Q. Qi, Y. Weng, C. Shen, Z. Cheng and S. He, *Nanoscale*, 2019, **11**, 11782–11788.
15 Z. Lou, M. Fujitsuka and T. Majima, *ACS Nano*, 2016, **10**, 6299–6305.
16 Z. Lou, M. Fujitsuka and T. Majima, *J. Phys. Chem. Lett.*, 2017, **8**, 844–849.
17 Z. Lou, S. Kim, M. Fujitsuka, X. Yang, B. Li and T. Majima, *Adv. Funct. Mater.*, 2018, **28**, 1706969.
18 J. W. Hong, D. H. Wi, S. Lee and S. W. Han, *J. Am. Chem. Soc.*, 2016, **138**, 15766–15773.
19 C. Y. Zhai, M. J. Sun, L. X. Zeng, M. Q. Xue, J. G. Pan, Y. K. Du and M. S. Zhu, *Appl. Catal., B*, 2019, **243**, 283–293; M. J. Sun, C. Y. Zhai, J. Y. Hu, M. S. Zhu and J. G. Pan, *J. Colloid Interface Sci.*, 2018, **511**, 110–118.
20 P. Wang, X. Zhang, J. Zhang, S. Wan, S. Guo, G. Lu, J. Yao and X. Huang, *Nat. Commun.*, 2017, **8**, 14580.
21 Y. Zhang, Z. Yin, H. Wang and X. F. Wu, *Org. Lett.*, 2019, **21**, 3242–3246.
22 A. M. Trzeciak and A. W. Augustyniak, *Coord. Chem. Rev.*, 2019, **384**, 1–20.
23 L. Zhang, N. Ding, L. Lou, K. Iwasaki, H. Wu, Y. Luo, D. Li, K. Nakata, A. Fujishima and Q. Meng, *Adv. Funct. Mater.*, 2019, **29**, 1806774.
24 J. Guo, Y. Zhang, L. Shi, Y. Zhu, M. F. Mideksa, K. Hou, W. Zhao, D. Wang, M. Zhao, X. Zhang, J. Lv, J. Zhang, X. Wang and Z. Tang, *J. Am. Chem. Soc.*, 2017, **139**, 17964–17972.
25 Z. Zheng, T. Tachikawa and T. Majima, *J. Am. Chem. Soc.*, 2014, **136**, 6870–6873.
26 L. Scarabelli, M. Coronado-Puchau, J. J. Giner-Casares, J. Langer and L. M. Liz-Marzan, *ACS Nano*, 2014, **8**, 5833–5842.
27 M. Zhou, M. Lin, L. Chen, Y. Wang, X. Guo, L. Peng, X. Guo and W. Ding, *Chem. Commun.*, 2015, **51**, 5116.
28 M. N. O'Brien, M. R. Jones, K. L. Kohlstedt, G. C. Schatz and C. A. Mirkin, *Nano Lett.*, 2015, **15**, 1012–1017.
29 H. Chen, F. Wang, K. Li, K. Woo, J. Wang, Q. Li, L. Sun, X. Zhang, H. Lin and C. Yan, *ACS Nano*, 2012, **6**, 7162–7171.
30 J. S. DuChene, G. Tagliabue, A. J. Welch, W. H. Cheng and H. A. Atwater, *Nano Lett.*, 2018, **18**, 2545–2550.
31 S. Y. Wang, Y. Y. Gao, S. Miao, T. F. Liu, L. C. Mu, R. G. Li, F. T. Fan and C. Li, *J. Am. Chem. Soc.*, 2017, **139**, 11771–11778.
32 Y. Shi, J. Wang, C. Wang, T. T. Zhai, W. J. Bao, J. J. Xu, X. H. Xia and H. Y. Chen, *J. Am. Chem. Soc.*, 2015, **137**, 7365–7370.
33 C. Boerigter, R. Campana, M. Morabito and S. Linic, *Nat. Commun.*, 2016, **7**, 10545.
34 T. Ouyang, Y. Ye, C. Wu and K. Xiao, *Angew. Chem., Int. Ed.*, 2019, **58**, 4923–4928.
35 C. Long, Y. Dai, Z. Gong and H. Jin, *Phys. Rev. B*, 2019, **99**, 115316.
36 C. Wang, X. G. Nie, Y. Shi, Y. Zhou, J. J. Xu, X. H. Xia and H. Y. Chen, *ACS Nano*, 2017, **11**, 5897–5905.
37 L. N. Zhou, D. F. Swearer, C. Zhang, H. Robatjazi, H. Q. Zhao, L. Henderson, L. L. Dong, P. Christopher, E. A. Carter, P. Nordlander and N. J. Halas, *Science*, 2018, **362**, 69–72.
38 Y. Zhu, Z. Zhang, N. Lu, R. Hua and B. Dong, *Chin. J. Catal.*, 2019, **40**, 413–423.